

Solar power conversion efficiency in modulated silicon nanowire photonic crystals

Alexei Deinega and Sajeesh John

Citation: *J. Appl. Phys.* **112**, 074327 (2012); doi: 10.1063/1.4752776

View online: <http://dx.doi.org/10.1063/1.4752776>

View Table of Contents: <http://jap.aip.org/resource/1/JAPIAU/v112/i7>

Published by the [American Institute of Physics](#).

Related Articles

Solar energy trapping with modulated silicon nanowire photonic crystals

J. Appl. Phys. **112**, 074326 (2012)

Hybrid pentacene/a-silicon solar cells utilizing multiple carrier generation via singlet exciton fission

Appl. Phys. Lett. **101**, 153507 (2012)

Light trapping in solar cells: Analytical modeling

Appl. Phys. Lett. **101**, 151105 (2012)

Performance of p- and n-side illuminated microcrystalline silicon solar cells following 2MeV electron bombardment

Appl. Phys. Lett. **101**, 143903 (2012)

Light trapping enhancements of inverted pyramidal structures with the tips for silicon solar cells

Appl. Phys. Lett. **101**, 141113 (2012)

Additional information on J. Appl. Phys.

Journal Homepage: <http://jap.aip.org/>

Journal Information: http://jap.aip.org/about/about_the_journal

Top downloads: http://jap.aip.org/features/most_downloaded

Information for Authors: <http://jap.aip.org/authors>

ADVERTISEMENT



The advertisement banner features a green background with abstract, flowing lines. At the top, the text "AIPAdvances" is displayed in a stylized font, with "AIP" in blue and "Advances" in green. Below this, the text "Special Topic Section:" is in white, followed by "PHYSICS OF CANCER" in large, bold, white capital letters. At the bottom, the text "Why cancer? Why physics?" is in yellow, and a blue button with the text "View Articles Now" is on the right.

Solar power conversion efficiency in modulated silicon nanowire photonic crystals

Alexei Deinega^{a)} and Sajeew John

Department of Physics, University of Toronto, 60 St. George Street, Toronto, Ontario, M5S 1A7, Canada

(Received 8 June 2012; accepted 20 July 2012; published online 12 October 2012)

It is suggested that using only $1\ \mu\text{m}$ of silicon, sculpted in the form of a modulated nanowire photonic crystal, solar power conversion efficiency in the range of 15%–20% can be achieved. Choosing a specific modulation profile provides antireflection, light trapping, and back-reflection over broad angles in targeted spectral regions for high efficiency power conversion without solar tracking. Solving both Maxwell's equations in the 3D photonic crystal and the semiconductor drift-diffusion equations in each nanowire, we identify optimal junction and contact geometries and study the influence of the nanowire surface curvature on solar cell efficiency. We demonstrate that suitably modulated nanowires enable 20% efficiency improvement over their straight counterparts made of an equivalent amount of silicon. We also discuss the efficiency of a tandem amorphous and crystalline silicon nanowire photonic crystal solar cell. Opportunities for "hot carrier" collection and up-conversion of infrared light, enhanced by photonic crystal geometry, facilitate further improvements in power efficiency. © 2012 American Institute of Physics. [<http://dx.doi.org/10.1063/1.4752776>]

I. INTRODUCTION

Crystalline silicon is the most widely used semiconductor in photovoltaics technology^{1–3} due to its abundance, non-toxicity, and good matching between its electronic bandgap and the solar spectrum. Silicon is an indirect-bandgap semiconductor with relatively low absorption in the near infrared. To compensate the wide variation of absorption length with wavelength, the thickness of silicon solar cells has typically been hundreds of microns. This leads to cost issues, since commercial high quality silicon is required to extend the carrier diffusion length to collect generated carriers before they can recombine. Thin film cells technology is one possible direction to reduce the cost, using a thin absorber layer.¹ Since carriers only have to be collected within a distance of a film thickness, poor quality silicon can be used. However, the efficiency of such cells is low because of significant reduction in light absorption. While typical efficiency of commercially available wafer-based silicon solar cells is 15%–20%, the best efficiency of thin-film silicon solar cells is around 10%.^{4,5}

Traditional methods to increase absorption inside solar cell include the use of antireflective quarter-wave layers or surface texturing.^{6,7} Antireflective surface textures have been studied for a wide range of size-to-wavelengths ratios combining numerical solution of Maxwell's equations with effective medium and geometric optics approximations in the long- and short- wavelength limits.⁷ Recently, photonic crystals have been considered in thin film photovoltaics for their ability to trap and localize the light.^{8–10} These include 1D, 2D,^{11–14} and 3D photonic crystals, consisting of different size gratings^{15,16} or nanohole arrays.^{16,17}

Another promising architecture consists of silicon nanowires.^{4,18} Here, one advantage is the use of a radial junction geometry where light absorption and carrier collection are decoupled, greatly increasing collection efficiency for silicon of poor quality.^{19–23} A second advantage is that silicon nanowire arrays can be designed to have very low reflectance and efficiently absorb incident light.^{24–27} Recently, sinusoidally modulated nanowires were proposed as a combination of nanowire and 3D photonic crystal geometries.²⁸ Such modulation can lead to strong light trapping effects due to the phenomenon of parallel interface refraction.²⁹

In this paper, we consider both optical and electronic properties of modulated nanowires and demonstrate their advantage relative to straight nanowires. We identify optimal junction and contact geometries and study the effect of the surface curvature on the power efficiency of resulting photonic crystal solar cell. We show that modulation of the nanowire surface leads to a baseline efficiency of 15% using only $1\ \mu\text{m}$ of equivalent bulk thickness of silicon. We also suggest an improved modulated nanowire using amorphous and crystalline silicon to form a tandem solar cell with 18.4% efficiency. The collection of hot carriers generated near the top of the nanowire and the reduction of nonradiative recombination near the contacts can lead to considerable further improvement in efficiency.

II. SOLAR ABSORPTION IN MODULATED NANOWIRE PHOTONIC CRYSTALS

As shown recently,²⁸ modulated silicon nanowires exhibit better solar absorption than their optimized straight counterparts. These modulated nanowires, arranged in a square lattice photonic crystal with period $a = 0.35\ \mu\text{m}$, consist of three sections (see Fig. 1). The top section is tapered in the form of a cone to provide an effective graded average refractive index for incoming light. Sinusoidal radial

^{a)}Electronic mail: deinega@physics.utoronto.ca.

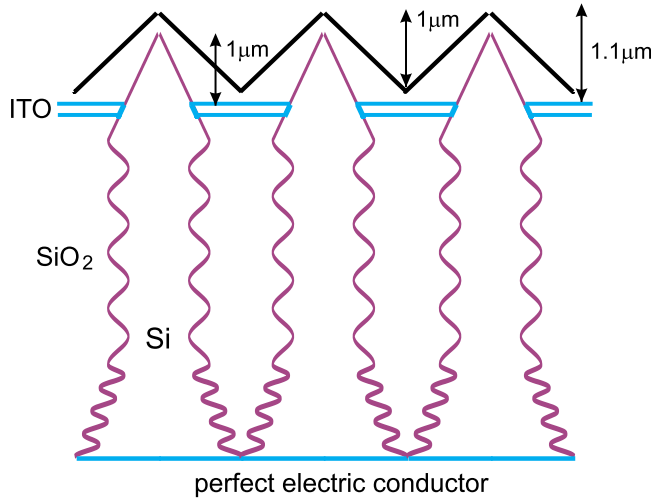


FIG. 1. Silicon nanowire array solar cell includes an ITO top contact and metallic back contact. The nanowires are embedded in a protective SiO_2 background which is textured at the top to reduce reflection of sunlight. Different scale for vertical and horizontal dimensions is used. Scale for texture and ITO is not preserved.

modulation of the middle section leads to a 3D simple cubic photonic crystal with enhanced photonic density of states in the solar spectrum. Coupling of sunlight to photonic modes from nearly any incident angle occurs through the phenomenon of parallel interface refraction.²⁹ The bottom section of the nanowire serves as a chirped photonic crystal back reflector for light not already absorbed in the upper sections.

For each section (Fig. 1), the nanowire radius as a function of vertical position z is given by $r(z) = a[r_0 + \frac{z}{h}(r_1 - r_0) + r_m \cos(2\pi z/a_z)]$, where r_0 and r_1 are radii at bottom and top section positions, r_m is amplitude of the modulation (r_0 , r_1 , and r_m are normalized to the period a), h is height of the section, and a_z is the lattice constant along z -axis. The coordinate z increases from 0 (bottom of the section) to h (top of the section). Parameters for each section are:

- (i) cone on the top of the nanowire to minimize reflection, $r_0 = 0.233 + 0.06$, $r_1 = 0$, $r_m = 0$ (no sinusoidal modulation), $h = 1.385 \mu\text{m}$;
- (ii) modulation in the middle to enable strong light trapping, $r_0 = r_1 = 0.233$, $r_m = 0.06$, $h = 2.92 \mu\text{m}$, $a_z = 0.73 \mu\text{m}$;
- (iii) a chirped modulation in the bottom to provide back reflection, $r_0 = 0.43$, $r_1 = 0.233$, $r_m = 0.06$, $h = 1.2 \mu\text{m}$, $a_z = 0.3 \mu\text{m}$.

The silicon nanowire photonic crystal is fully embedded in a textured silica slab (refractive index $n = 1.5$). This additional packaging in a silica background provides mechanical stability and protection to the overall device. The bottom metal contact is modelled as a perfect electric conductor which reflects all incoming light. The top contact is an indium tin oxide (ITO) film of the width 100 nm (refractive index $n = 1.8$) touching each nanowire cone (Fig. 1). This contact could be further architected into a Venetian blind geometry to further reduce reflection losses.³⁰

We calculate solar absorption inside the nanowire photonic crystal using the finite-difference time-domain (FDTD)

method³¹ with the help of Electromagnetic Template Library.³² We assume that the entire solar radiation is collapsed into a normal angle of incidence with linear polarization along the direction connecting neighboring nanowires (oblique incidence case can be simulated with the help of our FDTD iterative technique³³). We use the standard FDTD scheme, where a plane wave impulse is directed onto the nanowires array, fields are recorded, transformed to the frequency domain and normalized to the incident spectrum, to calculate frequency dependent absorption at each point \mathbf{r} inside a nanowire

$$\alpha(\omega, \mathbf{r}) = \frac{\omega \cdot \text{Im}(\epsilon) |\mathbf{E}(\omega, \mathbf{r})|^2}{c \cdot \text{Re}[\mathbf{E}_{\text{inc}}(\omega, \mathbf{r}), \mathbf{H}_{\text{inc}}^*(\omega, \mathbf{r})]}. \quad (1)$$

Here c is the speed of light in vacuum and ω is the frequency of light, ϵ is the silicon dielectric function.

We use a subpixel smoothing technique³⁴ to eliminate any staircase effect caused by our rectangular FDTD mesh. This technique significantly improves FDTD accuracy for arbitrary shaped scatterers. For reducing numerical reflection from the artificial absorbing perfectly matched layer (PML),³¹ we use additional back absorbing layers technique.³⁵ Experimental data on the silicon dielectric permittivity $\epsilon(\omega)$ is taken from Ref. 36. The frequency dependence of $\epsilon(\omega)$ is assigned in FDTD by considering a modified Lorentz approximation, where the dielectric polarization depends both on the electric field and its first time derivative.³⁷ This model provides an accurate fit to the response of crystalline silicon to sunlight over the wavelength range from 300 to 1000 nm, while conventional Debye, Drude, and Lorentz approximations fail.³⁷ Our fitting of the silicon dielectric function utilizes an open MATLAB program.³⁸

We assume that each absorbed photon of energy larger than the silicon electronic bandgap leads to generation of an electron-hole pair. The electrons and holes are assumed to rapidly lose energy by scattering from phonons and occupy energy levels near the conduction and valence band edges, respectively. Subsequently, the electron and hole dynamics is described by the drift-diffusion model.^{39,40} The total charge carrier generation rate is obtained by integration of the calculated absorption $\alpha(\lambda, \mathbf{r})$ with incident solar Air Mass 1.5 Global Spectrum⁴¹ intensity $I(\lambda)$ over the wavelength range of 350 – 1000 nm

$$G(\mathbf{r}) = \int_{\lambda_{\min}}^{\lambda_{\max}} \frac{\lambda}{hc} I(\lambda) \alpha(\lambda, \mathbf{r}) d\lambda. \quad (2)$$

Here photon energy is $\frac{hc}{\lambda}$, wavelength $\lambda = \frac{2\pi c}{\omega}$, h is the Planck's constant.

Since solar light is a sum of all possible polarizations, angular averaging

$$G(r, z) = \frac{1}{2\pi} \int_0^{2\pi} G(r \cos \varphi, r \sin \varphi, z) \cdot d\varphi, \quad (3)$$

is a good approximation for the solar generation rate $G(r \cos \varphi, r \sin \varphi, z)$.^{42,43}

The maximum achievable photocurrent density (MAPD), in which all generated carriers are assumed to be

collected, is calculated by integrating the generation rate (2) over the silicon nanowire volume V_s

$$\text{MAPD} = \int_{V_s} eG(\mathbf{r})d\mathbf{r}. \quad (4)$$

Here e is the electron charge. The case of 100% solar absorption over the 350 – 1000 nm range in crystalline silicon corresponds to $\text{MAPD} = 42.3 \text{ mA/cm}^2$.

In Fig. 2, we present the calculated absorption profile $\alpha(\lambda, r, z)$ for various wavelengths and the total generation rate $G(r, z)$ after angular averaging. Clearly, most of the bluish part of solar spectrum is absorbed in the nanocone, while longer wavelengths propagate to the modulated sections. MAPD for our modulated nanowire is 27.7 mA/cm^2 . For an optimized straight nanowire photonic crystal with $r=0.233$ and $h = 6.3 \mu\text{m}$ (height is chosen to use the same amount of silicon as for considered modulated nanowire) the MAPD drops to 20.7 mA/cm^2 in our solar cell geometry (Fig. 1).

III. ELECTRONIC PROPERTIES OF MODULATED NANOWIRES

To simulate photocurrent inside modulated nanowire, we simultaneously solve the Poisson equation and continuity equations for electrons and holes

$$\nabla^2\psi = -\frac{q}{\epsilon}(p - n + N_D - N_A), \quad (5)$$

$$\nabla J_n = -\nabla J_p = q(R - G), \quad (6)$$

$$J_n = qD_n\nabla n - q\mu_n n\nabla\psi, \quad (7)$$

$$J_p = -qD_p\nabla p - q\mu_p p\nabla\psi, \quad (8)$$

where ψ is the electrostatic potential, q is the elementary electronic charge, ϵ is the dielectric function, n and p are electron and hole densities, N_D and N_A are concentrations of ionized donors and acceptors, R and G are recombination

and generation rates, J_i , D_i , and μ_i are current densities, diffusion coefficients, and mobilities, $i = n, p$.

The generation rate profile, calculated using Eqs. (1) and (2), is used as an input to the continuity equations (6). Angular averaging of the generation rate (3) allows to reduce dimensionality of the problem from 3D (x, y, z) to 2D (r, z). To solve the Poisson and continuity equations numerically, we use zeroth order radial finite differences scheme.⁴²

In our calculations, we use silicon parameters found in Ref. 19.

- (i) doping concentration $N_d = N_a = 10^{18} \text{ cm}^{-3}$,
- (ii) electrons and holes mobility $\mu_n = 270 \text{ cm}^2 \text{ V}^{-1} \text{ s}^{-1}$, $\mu_p = 95 \text{ cm}^2 \text{ V}^{-1} \text{ s}^{-1}$,
- (iii) diffusion coefficient D_n, D_p is calculated using the Einstein relation $D = \frac{kT}{e} \mu$ (temperature T is assumed to be 300 K).

As in earlier literature,¹⁹ we consider only Shockley-Reed-Hall (SRH) recombination from a single-trap level at intrinsic Fermi level which lies near the middle of the bandgap

$$R = \frac{np - n_i^2}{\tau_p(n + n_i) + \tau_n(p + n_i)}, \quad (9)$$

where n_i is intrinsic charge carriers concentration. We choose the lifetime of the minority electrons in the p-region equal to the lifetime of minority holes in the n-region $\tau_n = \tau_p$. In the following, we consider the diffusion length $L_n = \sqrt{\tau_n D_n}$ as a independent variable. Including Auger and radiative recombination¹ in our model for R results primarily in a change of the diffusion length L_n . Rather than adding these other recombination channels into the microscopic expression (9), for simplicity we subsume these processes into the overall diffusion length L_n .

We impose surface recombination velocity of 100 cm s^{-1} at the Si-SiO₂ interface, as found in available experimental data.^{2,22} Contacts are assumed to be ohmic with a much larger surface recombination velocity of 10^5 cm s^{-1} , as found in Ref. 19.

We use highly doped region ($N_a = 5 \cdot 10^{18} \text{ cm}^{-3}$) with thickness 50 nm near bottom contact (back surface field). The interface between the higher and lower doped regions behaves like a p-n junction, where the resulting electric field makes a potential barrier to minority carrier flow to the surface.¹ This reduces the impact of the contact surface recombination on short circuit current density J_{sc} and open circuit voltage V_{oc} . As verified numerically, we find improvements on the order of 5% for our geometry compare to non-using back surface field.

We consider three different p-n junction geometries (Fig. 3):

- (i) “curved” radial junction. This junction consists of two parts: bottom horizontal part at the distance $0.1 \mu\text{m}$ from the bottom contact, and side part at the distance $0.05 \mu\text{m}$ from the modulated nanowire surface;
- (ii) straight radial junction which is obtained from curved radial junction by removing modulation;

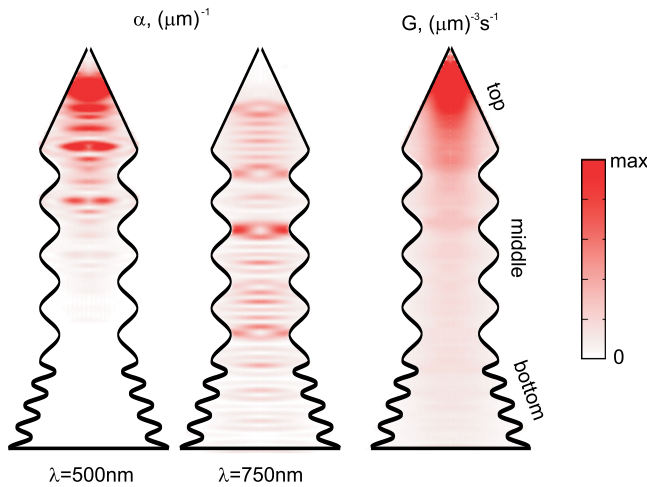


FIG. 2. Left, optical absorption profile inside modulated nanowire for chosen wavelengths (max = $10(\mu\text{m})^{-1}$, linear color bar scale). Right, corresponding carrier generation rate (2) (max = $10^{10}(\mu\text{m})^{-3}\text{s}^{-1}$, linear color bar scale). Averaging over polar angle ϕ is performed. Different scale for vertical and horizontal dimensions is used.

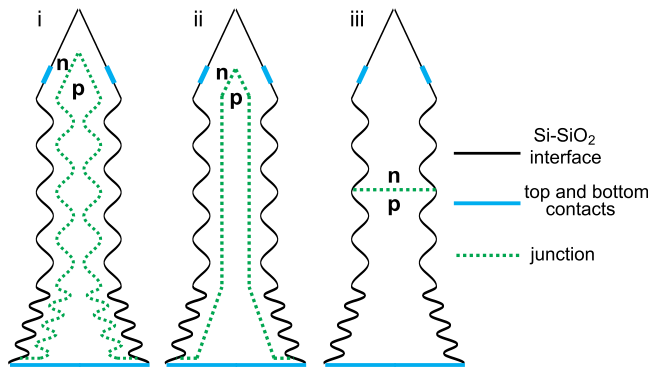


FIG. 3. (i) curved radial, (ii) straight radial, and (iii) axial junction geometries. Different scale for vertical and horizontal dimensions is used.

(iii) axial junction that separates nanowire by two layers of equal height.

Geometry (i) corresponds to the largest junction area, whereas geometry (iii) corresponds to the smallest one. As an illustration, we present the photocurrent distribution for the curved radial geometry in Fig. 4.

We calculate the short circuit current density J_{sc} (Fig. 5) and open circuit voltage V_{oc} (Fig. 6) for each of the three junction geometries. The short circuit current density J_{sc} is calculated as the current flux through the contact (bottom or top) normalized to the square lattice unit cell area $a \cdot a$.

The curved radial junction exhibits the highest value of J_{sc} in comparison to the straight radial and axial junctions (Fig. 5). In the latter two cases, generated carriers must traverse a longer distance to the junction where they become separated. The difference in J_{sc} for these three junctions

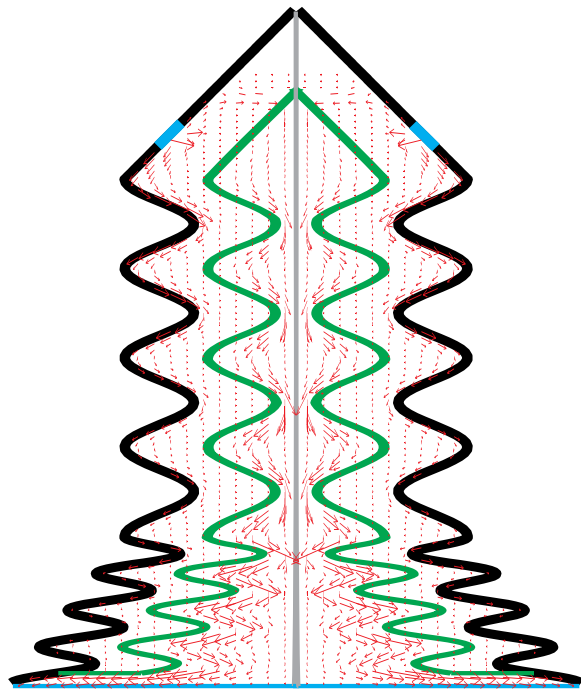


FIG. 4. Photocurrent density distribution inside modulated nanowire for curved radial junction geometry (for visualization purposes length of arrow corresponds to the photocurrent density multiplied by the distance from the nanowire axis). Different scale for vertical and horizontal dimensions is used.

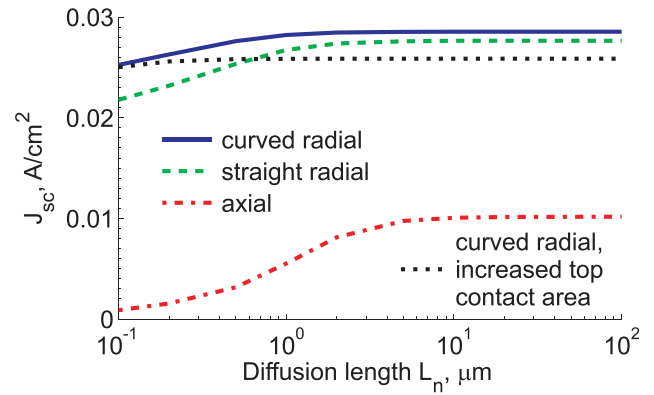


FIG. 5. Short circuit current density J_{sc} as a function of diffusion length L_n for different junction geometries. The curved radial junction yields the highest short circuit current density.

becomes smaller as the diffusion length, L_n , increases, and tends to nonzero constant value as $L_n \rightarrow \infty$. For high diffusion lengths most of the recombination occurs at the metal contacts. The curved radial junction yields the largest J_{sc} since carriers are more likely to “escape” recombination at the contacts and reach the junction where they become separated. At the same time, in the case of axial junction geometry, top contacts represent an obstacle for carriers generated at the top of the nanowire and moving to pn-junction, which negatively influences the photocurrent.

The axial junction provides the best open circuit voltage V_{oc} (Fig. 6), while results for curved and straight radial junctions are almost the same (we plot results only for curved radial junction). This can be explained by the negative influence of forward-bias recombination current¹ on the open circuit voltage V_{oc} . Forward-bias recombination current is caused by recombination of excess carriers at the depletion region. The value of this current is higher if the depletion (and therefore junction) region is more developed. Therefore, a less developed junction area produces a higher open circuit voltage V_{oc} . This explains higher values of V_{oc} for axial junction geometry compare with radial one.

The recombination current is inversely proportional to the carrier lifetime in the depletion region and therefore the silicon quality there. Consequently, using silicon of high quality in the depletion region around the junction improves

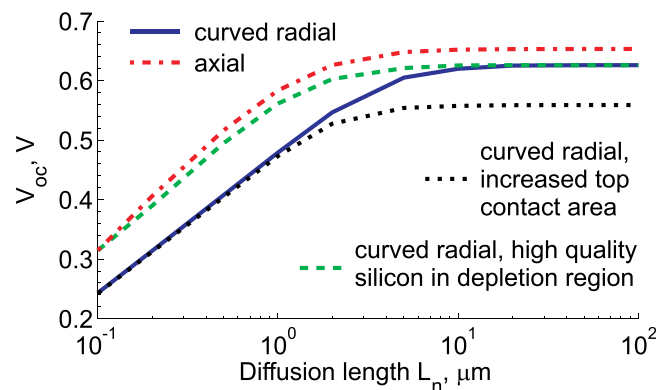


FIG. 6. Open circuit voltage V_{oc} as a function of diffusion length L_n for different junction geometries. The axial junction yields the highest open circuit voltage.

V_{oc} , even if the silicon quality elsewhere is small¹⁹ (but it does not influence J_{sc}). To demonstrate this we simulate the curved radial junction using a high diffusion length $L_n = 100 \mu\text{m}$ in the region 5 nm around the junction (Fig. 6).

Due to the small surface recombination velocity at the Si-SiO₂ interface (100 cm s^{-1}), the curvature of the nanowire surface does not influence J_{sc} and V_{oc} . Increasing the surface recombination velocity at the Si-SiO₂ interface from 100 cm s^{-1} to 1000 cm s^{-1} leads to only slight reduction in J_{sc} and V_{oc} (1%–2% for curved radial junction, $L_n = 100 \mu\text{m}$). Most of the surface recombination occurs at the contacts where the surface recombination velocity is about 10^5 cm s^{-1} . Therefore increasing the contact area will reduce J_{sc} and V_{oc} , since generated carriers are more likely to recombine at the contacts before reaching the junction. To demonstrate this, we simulate a curved radial junction assuming that the top contact covers the entire upper half surface of the nanowire $z \geq h_{tot}/2$, where h_{tot} is the nanowire height, and coordinate z increases from 0 (bottom of the nanowire), to h_{tot} (top of the nanowire) (see dotted curve at Figs. 5 and 6). On the other hand, changing the top contact position without changing its surface area has negligible influence on J_{sc} and V_{oc} , but only redistributes the photocurrent density.

We now compare the power conversion efficiency of solar cells based on modulated nanowires, straight nanowires ($r=0.233$, $h_{tot}=6.3 \mu\text{m}$, radial junction), and a planar cell ($h_{tot}=1.07 \mu\text{m}$). The height in both cases is chosen to use the same amount of silicon as in the modulated nanowires. We use a radial junction geometry for both types of nanowires. The generation rate for nanowires is obtained using an independent FDTD simulation of Maxwell's equations. We consider generation rate profiles obtained for the following geometries: nanowires are resting on (1) perfect electric conductor (as assumed before) or (2) semi-infinite quartz substrate (refractive index $n=1.5$). The generation rate for the planar cell is obtained using Beer's law for absorption and assuming no reflection from front (perfect antireflection coating) and back sides of the cell, as in Ref. 19. The calculated

efficiency as a function of diffusion length is plotted in Fig. 7. Results for the planar cell are in excellent agreement with results obtained analytically.¹⁹ Straight nanowires are much more efficient than the planar cell due to enhanced absorption and the use of the radial junction. The efficiency advantage is more significant for small diffusion length due to the radial junction. Modulation of the nanowire surface leads to further efficiency improvement because of better light trapping. Modulated nanowire solar cells improves the efficiency by about 10% or 20% relative to straight nanowires for cases when nanowires are resting on perfect electric conductor or quartz substrate correspondingly. Note that chosen parameters of the nanowire modulation are optimized for the second geometry case.²⁸ Use of the chirped modulation in the bottom part of the nanowire provides back reflection mechanism and prevents the light propagation into the quartz substrate. Modulation of the nanowire can be optimized for the first geometry as well to achieve higher efficiency.

In summary, using modulated nanowire solar cells improves the efficiency by about 20% relative to straight nanowires. The overall power conversion efficiency is about 15% provided that the diffusion length exceeds a few microns. Further improvements in efficiency are suggested below.

IV. EFFICIENCY ENHANCEMENTS

Nanowires can be synthesized using two materials with different lattice constants, and other parameters.^{44,45} This makes them suitable for tandem solar cells. Amorphous silicon and crystalline silicon have bandgaps well suited for tandem cells (1.7 eV and 1.12 eV, respectively). Such tandem cells have been studied previously for a planar geometry.⁴⁶ The absorption coefficient of amorphous silicon is about an order of magnitude greater than in crystalline silicon at visible wavelengths. However, amorphous silicon has poor transport properties with a short carrier diffusion length and carriers photogenerated in p or n layers are unlikely to contribute to the photocurrent. To overcome this problem a p-i-n junction with undoped or intrinsic region is used.¹ The built-

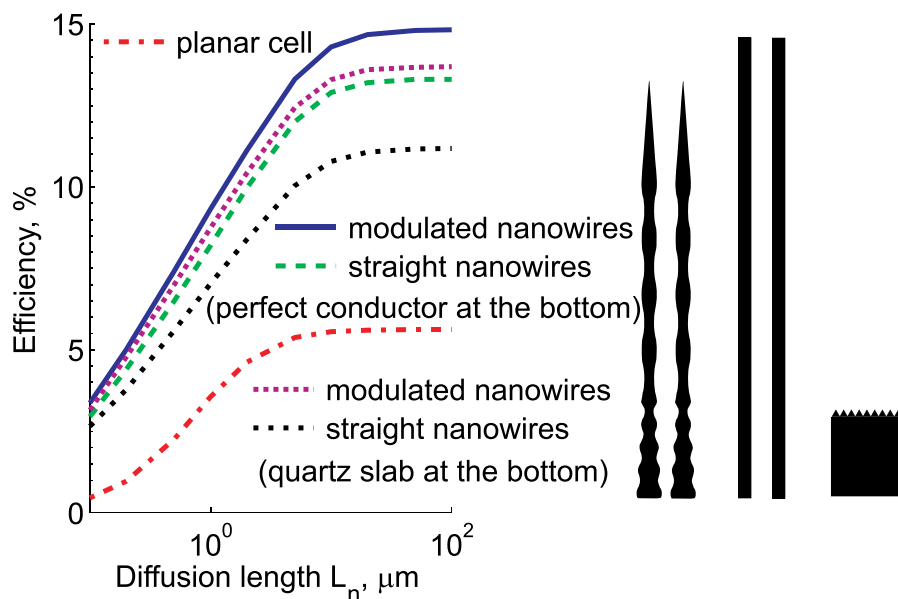


FIG. 7. Efficiency as a function of diffusion length L_n for different cells of the same volume of silicon (cell geometries are depicted on the right side). For the planar cell a perfect antireflection coating is assumed. A radial junction is used for the straight nanowire and a radial curved junction is used for modulated nanowire, see Fig. 3(i).

in bias is dropped across the undoped region, creating an electric field there. Carriers photogenerated in the undoped region are driven by this electric field to produce a photocurrent. Recently, the optical^{47–50} and electronic^{49–51} properties of amorphous silicon nanowires and nanocones have been studied.

In our geometry, it is advantageous to use an amorphous silicon region throughout the nanocone at the top of the nanowire. Our crystalline silicon nanowires already absorb 95% of photons with energy higher than the electronic bandgap of amorphous silicon. Therefore using amorphous silicon at the top of the nanowire does not increase the overall amount of absorbed sunlight. It simply redistributes the carrier generation profile along the nanowire. The height of the amorphous silicon segment is chosen such that the same amount of photocurrent is produced in the amorphous and crystalline silicon layers. Employing separate radial p-i-n and p-n junctions for each segment yields two solar cells connected in series within each nanowire. Adjacent n-doped and p-doped regions of these subcells can be heavily doped to form a tunnel junction between the subcells. Current passes through the tunnel junction between the subcells by quantum tunneling.¹ According to Kirchoff's law, photocurrent in the resulting tandem cell is equal to the photocurrent in each subcell, while the total voltage is a sum of subcell voltages. For a crystalline silicon subcell with radial junction we expect $V_{oc} = 0.62$ V (see Fig. 6), whereas for the amorphous silicon subcell we expect $V_{oc} = 0.9$ V, according to recent experimental^{49,50} and numerical⁵¹ results. Therefore, the total open circuit voltage is 1.52 V. Photocurrent in the tandem cell is one half that of the initial crystalline silicon nanowire cell, since the same amount of sunlight is absorbed by the two subcells. Therefore, we obtain a 22.6% efficiency improvement relative to the initial crystalline silicon nanowire, corresponding to a tandem cell with 18.4% efficiency.

Another way to improve the efficiency of modulated nanowires is by harnessing “hot” electrons before they lose energy by thermalization.^{1,3,52} One can see from Fig. 2 that a large fraction of high energy (blue and green) solar spectrum is absorbed in the nanocone segment of our nanowires. These high energy photons will produce hot carriers with energy far above the bottom of the electronic conduction band of silicon. Since hot carriers thermalization distances are typically of the order of tens of nanometers,³ such carriers can reach the top contact with incomplete thermalization.

Finally, we note that for diffusion lengths longer than the nanowire length, photogenerated carriers tend to recombine mostly at the contacts, since the surface recombination rate at the contacts is much higher than at Si-SiO₂ interface. If recombination at the contacts is radiative rather than non-radiative, this generated light can be coupled to photonic crystal modes, trapped inside nanowires array, and reabsorbed efficiently to regenerate electron-hole pairs. We estimate this effect indirectly by simulating decreased surface recombination at contacts. For modulated crystalline silicon nanowires with curved radial junction geometry, the efficiency improves from 15% to 20% if the surface recombination velocity at the contact is 100 cm s⁻¹ and diffusion length $L_n = 100$ μm. More accurate modelling of the photon

recycling effect requires coupling and self-consistency between the electromagnetic and electronic simulations.⁵³ The possibility of achieving small surface recombination velocity at the contacts by passivation with an intrinsic amorphous buffer layer has recently been presented.⁵⁴

In conclusion, modulated nanowire photonic crystals offer a number of opportunities for combined photonic and electronic management to greatly increase solar cell power conversion efficiency. Using only 1 μm of equivalent bulk thickness of silicon it is possible to achieve power conversion efficiencies in the range of 15%–20%, either matching or surpassing the efficiencies of solar cells requiring up to 300 μm of high quality silicon. A striking and unique feature of our modulated silicon nanowire photonic crystals is that their MAPD and efficiency remain nearly the same for sunlight incident over angles ranging from normal incidence to about 60° off-normal.²⁸ This implies that solar tracking by mechanical re-orientation of the solar cell is, for the most part, not required. This is particularly valuable for tandem solar cells where a current matching condition must be maintained between the subcells as the angle of direct solar illumination varies. The power conversion efficiency calculated in this paper represents only a baseline efficiency for photonic crystals consisting of 1 μm of silicon. Further enhancements in efficiency are likely to arise from “hot carrier” collection effects within the nano-cone regions of our solar cell design. Opportunities also arise from the “slow light” modes of our photonic crystal architecture. Such modes are known⁵⁵ to enhance nonlinear optical effects such as photon up-conversion and down-conversion.³ This type of solar spectrum reshaping within the photonic crystal likewise facilitates power efficiencies beyond the standard Shockley-Queisser limit³ of roughly 33%.

ACKNOWLEDGMENTS

This work is supported in part by the United States Department of Energy contract DE-FG02-10ER46754, the Natural Sciences and Engineering Research Council of Canada, and the Canadian Institute for Advanced Research.

¹J. Nelson, *The Physics of Solar Cells* (Imperial College, London, 2003).

²M. Green, *Silicon Solar Cells: Advanced Principles and Practice* (Centre for Photovoltaic Devices and Systems, Sydney, 1995).

³M. Green, *Third Generation Photovoltaics* (Springer, Berlin, 2006).

⁴*Nanotechnology for Photovoltaics*, edited by L. Tsakalakos (CRC, 2010).

⁵G. Beaucharne, “Silicon thin-film solar cells,” *Adv. OptoElectron.* **2007** (2007).

⁶H. A. Macleod, *Thin Film Optical Filter* (McGraw-Hill, New York, 1989).

⁷A. Deinega, I. Valuev, B. Potapkin, and Yu. Lozovik, “Minimizing light reflection from dielectric textured surfaces,” *JOSA A* **28**(5), 770–777 (2011).

⁸S. John, “Strong localization of photons in certain disordered dielectric superlattices,” *Phys. Rev. Lett.* **58**, 2486–2489 (1987).

⁹E. Yablonovitch, “Inhibited Spontaneous Emission in Solid-State Physics and Electronics,” *Phys. Rev. Lett.* **58**, 2059–2062 (1987).

¹⁰J. D. Joannopoulos, S. G. Johnson, J. N. Winn, and R. D. Meade, *Photonic Crystals: Molding the Flow of Light* (Princeton University, Princeton, NJ, 2008).

¹¹R. Dewan and D. Knipp, “Light trapping in thin-film silicon solar cells with integrated diffraction grating,” *J. Appl. Phys.* **106**, 074901 (2009).

¹²Q. G. Du, C. H. Kam, H. V. Demir, H. Y. Yu, and X. W. Sun, “Enhanced optical absorption in nanopatterned silicon thin films with a

- nano-cone-hole structure for photovoltaic applications," *Opt. Lett.* **36**, 1713–1715 (2011).
- ¹³Z. Yu, A. Raman, and S. Fan, "Nanophotonic light trapping theory for solar cells," *Appl. Phys. A* **105**, 329–339 (2011, Invited paper).
 - ¹⁴P. Wang and R. Menon, "Simulation and optimization of 1-D periodic dielectric nanostructures for light-trapping," *Opt. Express* **20**, 1849–1855 (2012).
 - ¹⁵R. B. Wehrspohn and J. Upping, "3D photonic crystals for photon management in solar cells," *J. Opt.* **14**, 024003 (2012).
 - ¹⁶K. A. Arpin, A. Mihi, H. T. Johnson, A. J. Baca, J. A. Rogers, J. A. Lewis, and P. V. Braun, "Multidimensional architectures for functional optical devices," *Adv. Mater.* **22**, 1084–1101 (2010).
 - ¹⁷P. Bermel, C. Luo, L. Zeng, L. C. Kimerling, and J. D. Joannopoulos, "Improving thin-film crystalline silicon solar cell efficiencies with photonic crystals," *Opt. Express* **15**, 16986–17000 (2007).
 - ¹⁸E. C. Garnett, M. L. Brongersma, Y. Cui, and M. D. Mc Gehee, "Nanowire solar cells," *Annu. Rev. Mater. Res.* **41**, 269–295 (2011).
 - ¹⁹B. M. Kayes, H. A. Atwater, and N. S. Lewis, "Comparison of the device physics principles of planar and radial p-n junction nanorod solar cells," *J. Appl. Phys.* **97**, 114302 (2005).
 - ²⁰B. Z. Tian, X. L. Zheng, T. J. Kempa, Y. Fang, N. F. Yu, G. H. Yu, J. L. Huang, and C. M. Lieber, "Coaxial silicon nanowires as solar cells and nanoelectronic power sources," *Nature (London)* **449**, 885 (2007).
 - ²¹L. Tsakalakos, J. Balch, J. Fronheiser, B. A. Korevaar, O. Sulima, and J. Rand, "Silicon nanowire solar cells," *Appl. Phys. Lett.* **91**, 233117 (2007).
 - ²²M. D. Kelzenberg, D. B. Turner-Evans, B. M. Kayes, M. A. Filler, M. C. Putnam, N. S. Lewis, and H. A. Atwater, "Photovoltaic measurements in single-nanowire silicon solar cells," *Nano Lett.* **8**, 710 (2008).
 - ²³Z. Fan, H. Razavi, J. Do, A. Moriwaki, O. Ergen, Y.-L. Chueh, P. W. Leu, J. C. Ho, T. Takahashi, L. A. Reichertz, S. Neale, K. Yu, M. Wu, J. W. Ager, and A. Javey, "Three dimensional nanopillar array photovoltaics on low cost and flexible substrates," *Nature Mater.* **8**, 648 (2009).
 - ²⁴L. Hu and G. Chen, "Analysis of optical absorption in silicon nanowire arrays for photovoltaic applications," *Nano Lett.* **7**(11), 3249–3252 (2007).
 - ²⁵J. S. Li, H. Y. Yu, S. M. Wong, X. C. Li, G. Zhang, P. G. Q. Lo, and D. L. Kwong, "Design guidelines of periodic Si nanowire arrays for solar cell application," *Appl. Phys. Lett.* **95**, 243113 (2009).
 - ²⁶C. Lin and M. L. Povinelli, "Optical absorption enhancement in silicon nanowire arrays with a large lattice constant for photovoltaic applications," *Opt. Express* **17**, 19371–19381 (2009).
 - ²⁷V. Sivakov, G. Andrä, A. Gawlik, A. Berger, J. Plentz, F. Falk, and S. H. Christiansen, "Silicon nanowire-based solar cells on glass: synthesis, optical properties, and cell parameters," *Nano Lett.* **9**(4), 1549–1554 (2009).
 - ²⁸G. Demésy, and S. John, "Solar energy trapping with modulated silicon nanowire photonic crystals," *J. Appl. Phys.* **112**, 074326 (2012).
 - ²⁹A. Chutinan and S. John, "Light trapping and absorption optimization in certain thin-film photonic crystal architectures," *Phys. Rev. A* **78**, 023825 (2008).
 - ³⁰P. Kuang, J.-M. Park, W. Leung, R. C. Mahadevapuram, K. S. Nalwa, T.-G. Kim, S. Chaudhary, K.-M. Ho, and K. Constant, "A new architecture for transparent electrodes: relieving the trade-off between electrical conductivity and optical transmittance," *Adv. Mater.* **23**, 2469–2473 (2011).
 - ³¹A. Taflov and S. H. Hagness, *Computational Electrodynamics: The Finite Difference Time-Domain Method* (Artech House, Boston, 2005).
 - ³²See <http://fdtd.kintechlab.com>, "Electromagnetic Template Library (EMTL)."
 - ³³I. Valuev, A. Deinega, and S. Belousov, "Iterative technique for analysis of periodic structures at oblique incidence in the finite-difference time-domain method," *Opt. Lett.* **33**, 1491–1493 (2008).
 - ³⁴A. Deinega and I. Valuev, "Subpixel smoothing for conductive and dispersive media in the FDTD method," *Opt. Lett.* **32**, 3429–3431 (2007).
 - ³⁵A. Deinega and I. Valuev, "Long-time behavior of PML absorbing boundaries for layered periodic structures," *Comput. Phys. Commun.* **182**, 149–151 (2011).
 - ³⁶M. A. Green and M. Keevers, "Optical properties of intrinsic silicon at 300 K," *Prog. Photovoltaics* **3**, 189–192 (1995).
 - ³⁷A. Deinega and S. John, "Effective optical response of silicon to sunlight in the finite-difference time-domain method," *Opt. Lett.* **37**, 112–114 (2012).
 - ³⁸See <http://fdtd.kintechlab.com/en/fitting>
 - ³⁹S. Selberherr, *Analysis and Simulation of Semiconductor Devices* (Springer, Springer-Verlag Wien, New York, 1984).
 - ⁴⁰R. Kircher and W. Bergner, *Three-Dimensional Simulation of Semiconductor Devices* (Birkhauser Verlag, 1991).
 - ⁴¹See <http://redc.nrel.gov/solar/spectra/am1.5> for open MATLAB program for fitting of arbitrary dielectric functions.
 - ⁴²A. Deinega and S. John, "Finite difference discretization of semiconductor drift-diffusion equations for nanowire solar cells," *Comput. Phys. Commun.* **183**, 2128 (2012).
 - ⁴³M. D. Kelzenberg, M. C. Putnam, D. B. Turner-Evans, N. S. Lewis, and H. A. Atwater, in *Proceedings of the 34th IEEE PVSC* (2009).
 - ⁴⁴F. Glas, "Critical dimensions for the plastic relaxation of strained axial heterostructures in free-standing nanowires," *Phys. Rev. B* **74**, 121302 (2006).
 - ⁴⁵A. Kandala, T. Betti, and A. Fontcuberta i Morral, "General theoretical considerations on nanowire solar cell designs," *Phys. Status Solidi A* **206**, 173–178 (2009).
 - ⁴⁶J. Meier, S. Dubail, S. Golay, U. Kroll, S. Fay, E. Vallat-Sauvain, L. Feitknecht, J. Dubail, and A. Shah, "Microcrystalline silicon and the impact on micromorph tandem solar cells," *Sol. Energy Mater. Sol. Cells* **74**, 457–467 (2002).
 - ⁴⁷J. Zhu, Z. Yu, G. F. Burkard, C. M. Hsu, S. T. Connor, Y. Xu, Q. Wang, M. McGehee, S. Fan, and Y. Cui, "Optical absorption enhancement in amorphous silicon nanowire and nanocone arrays," *Nano Lett.* **9**, 279 (2009).
 - ⁴⁸M. M. Adachi, M. P. Anantram, and K. S. Karim, "Optical properties of crystalline-amorphous core-SHELL silicon nanowires," *Nano Lett.* **10**, 4093–4098 (2010).
 - ⁴⁹J. Kim, A. J. Hong, J.-W. Nah, B. Shin, F. M. Ross, and D. K. Sadana, "Three-dimensional a-Si:H solar cells on glass nanocone arrays patterned by self-assembled Sn nanospheres," *ACS Nano* **6**, 265 (2012).
 - ⁵⁰C.-M. Hsu, C. Battaglia, C. Pahud, Z. Ruan, F.-J. Haug, S. Fan, C. Ballif, and Y. Cui, "High-efficiency amorphous silicon solar cell on a periodic nanocone back reflector," *Adv. Energy Mater.* **2**, 628 (2012).
 - ⁵¹Z. Pei, S.-T. Chang, C.-W. Liu, and Y.-C. Chen, "Numerical simulation on the photovoltaic behavior of an amorphous-silicon nanowire-array solar cell," *IEEE Electron Device Lett.* **30**, 1305–1307 (2009).
 - ⁵²G. Conibeer, R. Patterson, L. Huang, J.-F. Guillemoles, D. König, S. Shrestha, and M. A. Green, "Modelling of hot carrier solar cell absorbers," *Solar Energy Mater. Sol. Cells* **94**, 1516 (2010).
 - ⁵³J. L. Balenzateguia and A. Marti, "Detailed modelling of photon recycling: application to GaAs solar cells," *Solar Energy Mater. Sol. Cells* **90**, 1068–1088 (2006).
 - ⁵⁴P. J. Rostan, U. Rau, V. X. Nguyen, T. Kirchartz, M. B. Schubert, and J. H. Werner, "Low-temperature a-Si:H/ZnO/Al back contacts for high-efficiency silicon solar cell," *Solar Energy Mater. Sol. Cells* **90**, 1345 (2006).
 - ⁵⁵J. P. Mondia, H. M. van Driel, W. Jiang, A. R. Cowan, and J. F. Young, "Enhanced second-harmonic generation from planar photonic crystal," *Opt. Lett.* **28**, 2500–2502 (2003).